Orientation-dependent structural phase diagrams and dielectric properties of PbZr_{1−x}Ti_{x}O_{3} polydomain thin films

Ruijuan Xu, Jialan Zhang, Zuhuang Chen, and Lane W. Martin

Phys. Rev. B **91**, 144106 — Published 17 April 2015

DOI: 10.1103/PhysRevB.91.144106

Orientation-dependent structural phase diagrams and dielectric properties of $\mathbf{PbZr_{1-x}Ti_xO_3}$ polydomain thin films

Ruijuan Xu[1], Jialan Zhang[1], Zuhuang Chen[1], and Lane W. Martin[1,2*]
[1] *Department of Materials Science and Engineering,*
University of California, Berkeley, Berkeley, CA 94720 and
[2] *Materials Science Division, Lawrence Berkeley National Laboratory, Berkeley, CA 94720*

The orientation-dependent equilibrium ferroelectric domain structures and dielectric properties of polydomain $PbZr_{1-x}Ti_xO_3$ thin films are investigated using a phenomenological Ginzburg-Landau-Devonshire thermodynamic model. We develop and describe three-dimensional, polydomain models for (001)-, (101)-, and (111)-oriented films and explore the evolution of the structure and dielectric permittivity of the system as a function of epitaxial strain across the composition range $0.5 \leq x \leq 1.0$. Our studies reveal that the film orientation, epitaxial strain, and composition can combine in unexpected ways to drive exotic phase stability and transformations which have intriguing implications for the properties. In particular, in (101)- and (111)-oriented films, the application of epitaxial strains along non-$\langle 001 \rangle$-type crystallographic directions significantly reduces the stability range of the parent tetragonal phase (which is dominant in (001)-oriented films) and results in a variety of new symmetries. We also observe that the film orientation can be used to tune the relative fraction of intrinsic (*i.e.*, within a domain) and extrinsic (*i.e.*, from domain wall motion) contributions to the dielectric permittivity. Ultimately these studies reveal how composition, epitaxial strain, and film orientation provide for comprehensive control of the structure and properties of ferroelectrics.

I. INTRODUCTION

Advances in modern thin-film growth and characterization enable new modalities of strain control of ferroelectric materials that go beyond traditional lattice mismatch effects.[1,2] Recent experimental work has demonstrated that the control of film orientation is one promising and effective approach to manipulate ferroelectric domain structure and properties.[3,4] In studies of thin-film materials, such as the model ferroelectrics $PbZr_{1-x}Ti_xO_3$ and $BiFeO_3$, it has been noted that the variation of film orientation could result in exotic crystal and domain structures and give rise to enhanced ferroelectric susceptibilities.[5–8] In particular, recent work on (111)-oriented, tetragonal $PbZr_{0.2}Ti_{0.8}O_3$ films highlighted how domain-wall contributions to dielectric susceptibilities and ferroelectric switching characteristics can be dramatically tuned with film orientations.[7,8] In fact, varying the relative orientation of applied electric fields relative to the direction of polarization in ferroelectrics has been shown to give rise to enhanced dielectric and piezoelectric response and it has even been suggested that it could potentially giving rise to frustrated poling.[9–12]

The ultimate control of domain structure and properties, however, requires not only empirical observation, but the insights and understandings gleaned from theoretical simulations. To date the majority of theoretical models including Ginzburg-Landau-Devonshire theories and phase-field modeling have been developed to study the evolution of ferroelectric thin-film structures and properties that are tunable with strain, composition, temperature, and thickness.[13–20] Most of these studies, however, have focused on (001)-oriented heterostructures manifested in either monodomain or polydomain states. In fact, few studies have focused on systems of different orientations. For instance, thermodynamic calculations of (111)-oriented monodomain $PbTiO_3$ films, for instance, have predicted the presence of a dielectric anomaly in the paraelectric state that can be tailored from standard Curie-Weiss to diffuse-type by tuning the misfit strain.[21] Furthermore, recent first-principles calculations have suggested that a complex phase transition process, tuned by epitaxial strain, can occur in (111)-oriented $PbTiO_3$ and $BaTiO_3$ films[22] and that an unexpected triclinic phase and three distinct monoclinic phases may be possible in (110)-oriented $BaTiO_3$ films.[23] At the same time, for (101)-oriented $PbZr_{1-x}Ti_xO_3$ films with compositions near the morphotropic phase boundary, phase-field simulations suggest that mobile two-domain configurations can enhance piezoelectricity. Other phase-field simulations have also systematically studied the ferroelectric domain structures in (001)-, (101)-, and (111)-oriented $BiFeO_3$ films.[24] Despite these few examples, the vast majority of these studies focus on monodomain versions of materials which deviate from experimental (and practical) forms of these materials found in “thick” films (typically greater than just 25-50 nm) that exhibit a range of polydomain structures that result from a competition between elastic, electrostatic, domain wall, and other energies. In the prototypical ferroelectric $PbZr_{1-x}Ti_xO_3$ system, for instance, a comprehensive theoretical approach to understanding and systematically comparing the orientation-dependent domain structures, properties, and susceptibilities has not been undertaken.

In this work, we develop three-dimensional, polydomain phenomenological Ginzburg-Landau-Devonshire (GLD) thermodynamic models to produce orientation-, composition-, and strain-dependent phase diagrams that explore the evolution of structure and properties for thin films of the widely studied and technologically important tetragonal portion of the $\mathrm{PbZr}_{1-x}\mathrm{Ti}_x\mathrm{O}_3$ phase diagram. In particular, we study (001)-, (101)-, and (111)-oriented films and focus on the case of complex, polydomain phases in films above the critical thickness for domain formation. This work is accomplished by modifying the free-energy formalism for (001)-oriented heterostructures to allow for the construction of orientation-dependent, composition-strain phase diagrams for both (101)- and (111)-oriented films. We explore both phase and property (*i.e.*, dielectric permittivity) evolution for each film orientation. Our studies reveal that the film orientation, epitaxial strain, and composition can combine in unexpected ways to drive exotic phase stability and transformations which have intriguing implications for the properties of materials. The models suggest that the variation of film orientation can dramatically impact the energetics of the system and the application of epitaxial strains along non-⟨001⟩-type crystallographic directions significantly reduces the stability range of the parent tetragonal phase (which is dominant in (001)-oriented films) and results in a variety of new symmetries. We also observe that the film orientation can be used to tune the relative fraction of intrinsic (*i.e.*, within a domain) and extrinsic (*i.e.*, from domain wall motion) contributions to permittivity. This work has implications for the experimental design of ferroelectric heterostructures and could ultimately aid in the optimization of material response via a combination of film orientation, composition, and misfit strain control.

II. THERMODYNAMIC ANALYSIS

In the framework of the polydomain model, we consider epitaxial thin films of the ferroelectric $\mathrm{PbZr}_{1-x}\mathrm{Ti}_x\mathrm{O}_3$, which are grown in the cubic, paraelectric state on semi-infinite, cubic (001)-, (110)-, and (111)-oriented substrates, with a thickness greater than the critical thickness for domain formation. During cooling from the growth temperature the paraelectric-to-ferroelectric phase transition takes place, resulting in the formation of either a single domain or a polydomain state at lower temperatures. Here, to simplify the analysis, we neglect the strain accommodation by the generation of misfit dislocations and domain wall self-energy due to the rather small width of the domain wall structures as opposed to the film thickness (consistent to prior work on similar models).[14,15,27] Additionally, in the case of the thick films considered in our models, we also neglect polarization gradient effects near the substrate interface or film surface and, instead, assume homogeneous polarization and strains throughout the thickness of the film (again consistent with prior work in the field that assumes that the thickness of the interfacial layers is relatively small as compared to the total film thickness).[14,15,27] Additionally, we impose a short-circuit boundary condition to our system as would be present in a capacitor structure with high-carrier-density metal contacts, thereby negating the effects of depolarization fields.

For our formalism we utilize the Helmholtz free energy applicable to ferroelectric films with dense domain structures[14,15] to calculate the domain structures and dielectric susceptibilities as a function of substrate orientation and mismatch strain. The Helmholtz free energy F is derived from the Legendre transformation of the Gibbs free energy G via $F = G + \sum_{n=1}^{6} \sigma_n S_n$. In the crystallographic reference frame X (x_1, x_2, x_3) with x_1, x_2, and x_3 along [100], [010], and [001], respectively, the Gibbs free energy G and the modified Helmholtz free energy density $\tilde{F}$ can be written in terms of the polarization P_i and stresses n as[14,25]

$$\begin{aligned}
G = {} & \alpha_1(P_1^2+P_2^2+P_3^2)+\alpha_{11}(P_1^4+P_2^4+P_3^4) \\
& +\alpha_{12}(P_1^2P_2^2+P_2^2P_3^2+P_1^2P_3^2)+\alpha_{111}(P_1^6+P_2^6+P_3^6) \\
& +\alpha_{112}[P_1^4(P_2^2+P_3^2)+P_2^4(P_3^2+P_1^2)+P_3^4(P_1^2+P_2^2)] \\
& +\alpha_{123}P_1^2P_2^2P_3^2-1/2s_{11}(\sigma_1^2+\sigma_2^2+\sigma_3^2) \\
& -s_{12}(\sigma_1\sigma_2+\sigma_2\sigma_3+\sigma_1\sigma_3)-1/2s_{44}(\sigma_4^2+\sigma_5^2+\sigma_6^2) \\
& -Q_{11}(\sigma_1P_1^2+\sigma_2P_2^2+\sigma_3P_3^2) \\
& -Q_{12}[\sigma_1(P_2^2+P_3^2)+\sigma_3(P_1^2+P_2^2)+\sigma_2(P_1^2+P_2^2)] \\
& -Q_{44}(P_2P_3\sigma_4+P_1P_3\sigma_5+P_2P_1\sigma_6)
\end{aligned} \tag{1}$$

$$\begin{aligned}
\tilde{F} = {} & \alpha_1(P_1^2+P_2^2+P_3^2)+\alpha_{11}(P_1^4+P_2^4+P_3^4) \\
& +\alpha_{12}(P_1^2P_2^2+P_2^2P_3^2+P_1^2P_3^2)+\alpha_{111}(P_1^6+P_2^6+P_3^6) \\
& +\alpha_{112}[P_1^4(P_2^2+P_3^2)+P_2^4(P_3^2+P_1^2)+P_3^4(P_1^2+P_2^2)] \\
& +\alpha_{123}P_1^2P_2^2P_3^2+\frac{1}{2}s_{11}(\sigma_1^2+\sigma_2^2+\sigma_3^2) \\
& +s_{12}(\sigma_1\sigma_2+\sigma_2\sigma_3+\sigma_1\sigma_3)+\frac{1}{2}s_{44}(\sigma_4^2+\sigma_5^2+\sigma_6^2) \\
& -\frac{1}{2}\varepsilon_0\left(E_1^2+E_2^2+E_3^2\right)-E_1P_1-E_2P_2-E_3P_3
\end{aligned} \tag{2}$$

where α_1, α_{ij}, and α_{ijk} are the dielectric stiffnesses at constant stress, s_{mn} are the elastic compliances at constant polarization, Q_{ij} are the electrostrictive constants of the paraelectric phase, and E_i are the components of external electric field in the film. The values of the above coefficients are provided in Table I.[26]

In order to apply the proper mechanical boundary conditions and to simplify the analyses for (101)- and (111)-orientations, we introduce new crystallographic reference frames for both cases. For (101)-oriented films, we use the crystallographic reference frame X' (x_1', x_2', x_3') where x_1', x_2', and x_3' correspond to the [$\bar{1}$01], [0$\bar{1}$0], and [101] of reference frame X. Likewise for (111)-oriented films we define reference frame X'' (x_1'', x_2'', x_3'') where x_1'', x_2'', and x_3'' correspond to the [1$\bar{1}$0], [11$\bar{2}$], and [111] of reference frame X. In both the X' and X'' reference frames x_3',

x_3'' are defined to be perpendicular to the plane of the film and x_1' (x_2'), x_1'' (x_2'') are aligned in the plane of the film. Thus the free energy (G and $\tilde{F}$) can be rewritten as G' and $\tilde{F}'$ or G'' and $\tilde{F}''$ in terms of P_i', σ_n' and P_i'',$''_n$ in the reference frame X' and X'' using the following transformation matrices t_{ij}' and t_{ij}'', respectively:[20,23]

$$\begin{bmatrix} -\frac{1}{\sqrt{2}} & 0 & \frac{1}{\sqrt{2}} \\ 0 & -1 & 0 \\ \frac{1}{\sqrt{2}} & 0 & \frac{1}{\sqrt{2}} \end{bmatrix} \tag{3}$$

$$\begin{bmatrix} \frac{1}{\sqrt{2}} & -\frac{1}{\sqrt{2}} & 0 \\ \frac{1}{\sqrt{6}} & \frac{1}{\sqrt{6}} & -\frac{2}{\sqrt{6}} \\ \frac{1}{\sqrt{3}} & \frac{1}{\sqrt{3}} & \frac{1}{\sqrt{3}} \end{bmatrix} \tag{4}$$

P_i and σ_n in the reference frame X can be expressed in terms of P_i', σ_i' and P_i'', σ_i'' in the reference frames X' and X'', respectively, via the relation $\mathbf{P} = \left(t_{ij}'\right)^{-1}\mathbf{P}'$, $\mathbf{K} = \left(t_{ij}'\right)^{-1} \cdot \mathbf{K}' \cdot t_{ij}'$ and $\mathbf{P} = \left(t_{ij}''\right)^{-1}\mathbf{P}''$, $\mathbf{K} = \left(t_{ij}''\right)^{-1} \cdot \mathbf{K}'' \cdot t_{ij}''$, where $\mathbf{P}$, $\mathbf{P}'$, and $\mathbf{P}''$ are polarization and $\mathbf{K}$, $\mathbf{K}'$, and $\mathbf{K}''$ are stress tensor matrices in the reference frames X, X', and X'', respectively. Thus the free energy $\tilde{F}$ can be transformed to free energy $\tilde{F}'$ and $\tilde{F}''$ in terms of P_i', σ_i' and P_i'', σ_i'' in the reference frames X' and X'', where P_1', P_2', and P_3' and P_1'', P_2'', and P_3'' are along x_1', x_2', and x_3' and x_1'', x_2'', and x_3'' in reference frames X' and X'', respectively. The explicit formalism of $\tilde{F}'$ and $\tilde{F}''$ are rather complex and thus for brevity we provide those in simplified form in equations (4) and (5) using $\widetilde{\mathbf{P}}'$, $\widetilde{\mathbf{K}}'$ and $\widetilde{\mathbf{P}}''$, $\widetilde{\mathbf{K}}''$ to represent the matrices $\left(t_{ij}'\right)^{-1}\mathbf{P}'$, $\left(t_{ij}'\right)^{-1} \cdot \mathbf{K}' \cdot t_{ij}'$ and $\left(t_{ij}''\right)^{-1}\mathbf{P}''$, $\left(t_{ij}''\right)^{-1} \cdot \mathbf{K}'' \cdot t_{ij}''$, respectively:

TABLE I: Values of thermodynamic coefficients for PbZr$_{1-x}$Ti$_x$O$_3$ (x = 0.5, 0.6, 0.7, 0.8 ,0.9, 1.0) used in the Ginzburg-Landau-Devonshire modeling at T = 300 K.

Parameters	0.5	0.6	0.7	0.8	0.9	1.0
$a_1(10^8 C^{-2}{\cdot}m^2{\cdot}N)$	-0.49	-0.83	-1.24	-1.49	-1.64	-1.75
$a_{11}(10^7 C^{-4}{\cdot}m^6{\cdot}N)$	4.76	3.61	0.65	-3.05	-5.85	-7.25
$a_{12}(10^8 C^{-4}{\cdot}m^6{\cdot}N)$	1.74	3.23	5.11	6.32	7.06	7.50
$a_{111}(10^8 C^{-6}{\cdot}m^{10}{\cdot}N)$	1.34	1.86	2.35	2.48	2.52	2.60
$a_{112}(10^8 C^{-6}{\cdot}m^{10}{\cdot}N)$	6.13	8.50	10.25	9.68	8.10	6.10
$a_{123}(10^9 C^{-6}{\cdot}m^{10}{\cdot}N)$	-2.89	-4.06	-5.00	-4.90	-4.36	-3.66
$s_{11}(10^{-12} N{\cdot}m^{-2})$	10.5	8.60	8.40	8.20	8.10	8.00
$s_{12}(10^{-12} N{\cdot}m^{-2})$	-3.70	-2.80	-2.70	-2.60	-2.50	-2.50
$s_{44}(10^{-12} N{\cdot}m^{-2})$	28.7	21.2	17.5	14.4	12.0	9.00
$T_c^{\infty}(K)$	665.6	691.4	713.2	732.1	750.1	765.1

$$\begin{aligned}
\widetilde{F}' = {} & \alpha_1 \left(\mathbf{P}'^2_{1,1} + \mathbf{P}'^2_{2,1} + \mathbf{P}'^2_{3,1}\right) + \alpha_{11} \left(\mathbf{P}'^4_{1,1} + \mathbf{P}'^4_{2,1} + \mathbf{P}'^4_{3,1}\right) \\
& + \alpha_{12} \left(\mathbf{P}'^2_{1,1}\mathbf{P}'^2_{2,1} + \mathbf{P}'^2_{2,1}\mathbf{P}'^2_{3,1} + \mathbf{P}'^2_{1,1}\mathbf{P}'^2_{3,1}\right) \\
& + \alpha_{111} \left(\widetilde{\mathbf{P}}'^6_{1,1} + \widetilde{\mathbf{P}}'^6_{2,1} + \widetilde{\mathbf{P}}'^6_{3,1}\right) + \alpha_{112} \left[\widetilde{\mathbf{P}}'^4_{1,1} \left(\widetilde{\mathbf{P}}'^2_{2,1} + \widetilde{\mathbf{P}}'^2_{3,1}\right)\right. \\
& \left. + \widetilde{\mathbf{P}}'^4_{2,1} \left(\widetilde{\mathbf{P}}'^2_{3,1} + \widetilde{\mathbf{P}}'^2_{1,1}\right) + \widetilde{\mathbf{P}}'^4_{3,1} \left(\widetilde{\mathbf{P}}'^2_{1,1} + \widetilde{\mathbf{P}}'^2_{2,1}\right)\right] \\
& + \alpha_{123}\widetilde{\mathbf{P}}'^2_{1,1}\widetilde{\mathbf{P}}'^2_{2,1}\widetilde{\mathbf{P}}'^2_{3,1} + \frac{1}{2}s_{11} \left(\widetilde{\mathbf{K}}'^2_{1,1} + \widetilde{\mathbf{K}}'^2_{2,2} + \widetilde{\mathbf{K}}'^2_{3,3}\right) \\
& + s_{12} \left(\widetilde{\mathbf{K}}'_{1,1}\widetilde{\mathbf{K}}'_{2,2} + \widetilde{\mathbf{K}}'_{2,2}\widetilde{\mathbf{K}}'_{3,3} + \widetilde{\mathbf{K}}'_{1,1}\widetilde{\mathbf{K}}'_{3,3}\right) \\
& + \frac{1}{2}s_{44} \left(\widetilde{\mathbf{K}}'^2_{2,3} + \widetilde{\mathbf{K}}'^2_{1,3} + \widetilde{\mathbf{K}}'^2_{1,2}\right) - \frac{1}{2}\varepsilon_0 \left(E_1'^2 + E_2'^2 + E_3'^2\right) \\
& - E_1'P_1' - E_2'P_2' - E_3'P_3'
\end{aligned} \tag{5}$$

$$\begin{aligned}
\widetilde{F}'' = {} & \alpha_1 \left(\mathbf{P}''^2_{1,1} + \mathbf{P}''^2_{2,1} + \mathbf{P}''^2_{3,1}\right) + \alpha_{11} \left(\mathbf{P}''^4_{1,1} + \mathbf{P}''^4_{2,1} + \mathbf{P}''^4_{3,1}\right) \\
& + \alpha_{12} \left(\mathbf{P}''^2_{1,1}\mathbf{P}''^2_{2,1} + \mathbf{P}''^2_{2,1}\mathbf{P}''^2_{3,1} + \mathbf{P}''^2_{1,1}\mathbf{P}''^2_{3,1}\right) \\
& + \alpha_{111} \left(\widetilde{\mathbf{P}}''^6_{1,1} + \widetilde{\mathbf{P}}''^6_{2,1} + \widetilde{\mathbf{P}}''^6_{3,1}\right) + \alpha_{112} \left[\widetilde{\mathbf{P}}''^4_{1,1} \left(\widetilde{\mathbf{P}}''^2_{2,1} + \widetilde{\mathbf{P}}''^2_{3,1}\right)\right. \\
& \left. + \widetilde{\mathbf{P}}''^4_{2,1} \left(\widetilde{\mathbf{P}}''^2_{3,1} + \widetilde{\mathbf{P}}''^2_{1,1}\right) + \widetilde{\mathbf{P}}''^4_{3,1} \left(\widetilde{\mathbf{P}}''^2_{1,1} + \widetilde{\mathbf{P}}''^2_{2,1}\right)\right] \\
& + \alpha_{123}\widetilde{\mathbf{P}}''^2_{1,1}\widetilde{\mathbf{P}}''^2_{2,1}\widetilde{\mathbf{P}}''^2_{3,1} + \frac{1}{2}s_{11} \left(\widetilde{\mathbf{K}}''^2_{1,1} + \widetilde{\mathbf{K}}''^2_{2,2} + \widetilde{\mathbf{K}}''^2_{3,3}\right) \\
& + s_{12} \left(\widetilde{\mathbf{K}}''_{1,1}\widetilde{\mathbf{K}}''_{2,2} + \widetilde{\mathbf{K}}''_{2,2}\widetilde{\mathbf{K}}''_{3,3} + \widetilde{\mathbf{K}}''_{1,1}\widetilde{\mathbf{K}}''_{3,3}\right) \\
& + \frac{1}{2}s_{44} \left(\widetilde{\mathbf{K}}''^2_{2,3} + \widetilde{\mathbf{K}}''^2_{1,3} + \widetilde{\mathbf{K}}''^2_{1,2}\right) - \frac{1}{2}\varepsilon_0 \left(E_1''^2 + E_2''^2 + E_3''^2\right) \\
& - E_1''P_1'' - E_2''P_2'' - E_3''P_3''
\end{aligned} \tag{6}$$

where E_i' and E_i'' are components of external electric field in the reference frames X' and X''. The complete, explicit formalisms for both $\tilde{F}'$ and $\tilde{F}''$ are provided in the Supplemental Materials. For polydomain structures, the thermodynamic equilibrium state can be described by the average free-energy density $\left\langle \tilde{F} \right\rangle$ which can be written as $\left\langle \tilde{F} \right\rangle = \sum\limits_{k=1}^{n} \phi_k F_k$, $\left\langle \tilde{F}' \right\rangle = \sum\limits_{k=1}^{n} \phi'_k F'_k$, and $\left\langle \tilde{F}'' \right\rangle = \sum\limits_{k=1}^{n} \phi''_k F''_k$ for the (001)-, (101)-, and (111)-oriented films, respectively. In these equations, ϕ_k (ϕ_k' or ϕ_k'') are the volume fraction of the k^{th} domain type and F_k (F_k' or F_k'') are the energy density within the k^{th} domain. It is possible to eliminate the stresses σ ($\sigma_n{}'$ or $\sigma_n{}''$) from the $\left\langle \tilde{F} \right\rangle$ ($\left\langle \tilde{F}' \right\rangle$ or $\left\langle \tilde{F}'' \right\rangle$) using the following mechanical boundary conditions:

(001)-oriented films:

$$\langle S_1 \rangle = \sum_{k=1}^{n} \phi_k S_1^k = u_m, \langle S_2 \rangle = \sum_{k=1}^{n} \phi_k S_2^k = u_m,$$

$$\langle S_6 \rangle = \sum_{k=1}^{n} \phi_k S_6^k = 0, \tag{7}$$

$$\langle \sigma_3 \rangle = \langle \sigma_4 \rangle = \langle \sigma_5 \rangle = 0, \tag{8}$$

(101)-oriented films:

$$\langle S_1' \rangle = \sum_{k=1}^{n} \phi_k' S_1'^k = u_m', \langle S_2' \rangle = \sum_{k=1}^{n} \phi_k' S_2'^k = u_m',$$

$$\langle S_6' \rangle = \sum_{k=1}^{n} \phi_k' S_6'^k = 0, \tag{9}$$

$$\langle \sigma_3' \rangle = \langle \sigma_4' \rangle = \langle \sigma_5' \rangle = 0, \tag{10}$$

(111)-oriented films:

$$\langle S_1'' \rangle = \sum_{k=1}^{n} \phi_k'' S_1''^k = u_m'', \langle S_2'' \rangle = \sum_{k=1}^{n} \phi_k'' S_2''^k = u_m'',$$

$$\langle S_6'' \rangle = \sum_{k=1}^{n} \phi_k'' S_6''^k = 0, \tag{11}$$

$$\langle \sigma_3'' \rangle = \langle \sigma_4'' \rangle = \langle \sigma_5'' \rangle = 0, \tag{12}$$

where S_n^k ($S_n'^k$ and $S_n''^k$) refers to the strain components in the k^{th} domain which can be derived from $S_n = -\partial G/\partial \sigma_n$ ($S_n' = -\partial G'/\partial \sigma_n'$ or $S_n'' = -\partial G''/\partial \sigma_n''$) and u_m (u_m' or u_m'') refers to the in-plane misfit strain with respect to the growth plane. In polydomain films, these macroscopic conditions must be supplemented by the microscopic boundary conditions related to the presence of the domain walls. To achieve this, we create a local reference frame Y (y_1, y_2, y_3) with y_3 perpendicular to the domain walls and thus the strain compatibility in the neighboring domains implies

$$S_{n'}^k = S_{n'}^{k+1} (S_{n'}'^k = S_{n'}'^{k+1} or S_{n'}''^k = S_{n'}''^{k+1}) (n = 1, 2, 6) \tag{13}$$

and the mechanical equilibrium of the domains implies that the stress components are related as

$$\sigma_{n'}^k = \sigma_{n'}^{k+1} (\sigma_{n'}'^k = \sigma_{n'}'^{k+1} or \sigma_{n'}''^k = \sigma_{n'}''^{k+1}) (n = 3, 4, 5). \tag{14}$$

In addition, we can set the average electric field $\langle E_i \rangle$ ($\langle E_i' \rangle$ or $\langle E_i'' \rangle$) to be zero in the case of the short-circuit boundary conditions and in the absence of a depolarization field. The microscopic electric field continuity equation thus yields the following boundary conditions:

$$E_{1'}^k = E_{1'}^{k+1} (E_{1'}'^k = E_{1'}'^{k+1} or E_{1'}''^k = E_{1'}''^{k+1}), \tag{15}$$

$$E_{2'}^k = E_{2'}^{k+1} (E_{2'}'^k = E_{2'}'^{k+1} or E_{2'}''^k = E_{2'}''^{k+1}), \tag{16}$$

$$\begin{aligned} &\varepsilon_0 E_{3'}^k + P_{3'}^k = \varepsilon_0 E_{3'}^{k+1} + P_{3'}^{k+1} \\ &(\varepsilon_0 E_{3'}'^k + P_{3'}'^k = \varepsilon_0 E_{3'}'^{k+1} + P_{3'}'^{k+1} or \\ &\varepsilon_0 E_{3'}''^k + P_{3'}''^k = \varepsilon_0 E_{3'}''^{k+1} + P_{3'}''^{k+1}). \end{aligned} \tag{17}$$

The above relations make it possible to rewrite the free-energy density for each film orientation in terms of polarization components P_i^k ($P_i'^k$ or $P_i''^k$) and domain volume fractions ϕ_k (ϕ_k' or ϕ_k''). Performing the minimization of $\left\langle \tilde{F} \right\rangle$ ($\left\langle \tilde{F}' \right\rangle$ and $\left\langle \tilde{F}'' \right\rangle$), we can find the equilibrium polarizations and domain populations as a function of mismatch strain ($u_m = (a_s - a_p)/a_s$, where a_s is the lattice parameter of the substrate and a_p is the lattice parameter of the cubic paraelectric phase of the film)[27] for the respective film orientations.

Our thermodynamic theory also allows us to calculate the out-of-plane dielectric permittivity ($\varepsilon_\perp$, $\varepsilon_\perp'$, $\varepsilon_\perp''$ for (001)-, (101)-, and (111)-oriented films, respectively) as the sum of the intrinsic (the first term) and the motional extrinsic (the second term) contributions as

$$\varepsilon_\perp = \sum_k \phi_k \frac{dP_3}{dE_3} + \sum_k P_3^k \frac{d\phi_3}{dE_3}, \tag{18}$$

$$\varepsilon_\perp' = \sum_k \phi_k' \frac{dP_3'}{dE_3'} + \sum_k P_3'^k \frac{d\phi_3'}{dE_3'}, \tag{19}$$

$$\varepsilon_\perp'' = \sum_k \phi_k'' \frac{dP_3''}{dE_3''} + \sum_k P_3''^k \frac{d\phi_3''}{dE_3''}. \tag{20}$$

Here the intrinsic dielectric susceptibility can be described as the reversible variation of polarization P_i (P_i' or P_i'') with varying electric field E_j (E_j' or E_j'') $\chi_{ij} = \frac{dP_i}{dE_j}$ ($\chi_{ij}' = \frac{dP_i'}{dE_j'}$ or $\chi_{ij}'' = \frac{dP_i''}{dE_j''}$). With the relation $E_i = \frac{d\tilde{F}}{dP_i}$ ($E_i' = \frac{d\tilde{F}'}{dP_i'}$ or $E_i'' = \frac{d\tilde{F}''}{dP_i''}$), we can further use differentiation of free energy to derive the expression for the dielectric susceptibility. Using the inversion of the reciprocal dielectric susceptibility matrix ($\mathbf{\Theta} = [\eta_{ij}]$, $\mathbf{\Theta}' = \left[\eta_{ij}'\right]$, $\mathbf{\Theta}'' = \left[\eta_{ij}''\right]$ for (001)-, (101)-, and (111)-oriented films, respectively, where $\eta_{ij} = \frac{\partial^2 \tilde{F}}{\partial P_i \partial P_j}$ and $\eta_{ij}' = \frac{\partial^2 \tilde{F}'}{\partial P_i' \partial P_j'}$ and $\eta_{ij}'' = \frac{\partial^2 \tilde{F}''}{\partial P_i'' \partial P_j''}$), we find the dielectric susceptibility as $\chi_{ij} = \mathbf{\Theta}_{i,j}^{-1}$ ($\chi_{ij}' = \mathbf{\Theta}_{i,j}'^{-1}$ or $\chi_{ij}'' = \mathbf{\Theta}_{i,j}''^{-1}$) and thus the relative intrinsic dielectric permittivity as $\varepsilon_{ij}^{int} = \chi_{ij} + 1$ ($\varepsilon_{ij}^{int\prime} = \chi_{ij}' + 1$ or $\varepsilon_{ij}^{int\prime\prime} = \chi_{ij}'' + 1$). For the film geometry considered in this work, we will only study the out-of-plane dielectric permittivity (ε_{33}^{int}, $\varepsilon_{33}^{int\prime}$, $\varepsilon_{33}^{int\prime\prime}$) using the explicit expression for dielectric permittivity obtained by performing the inversion of the reciprocal dielectric susceptibility matrix ($\varepsilon_{33}^{int} = \frac{(\eta_{11}+\eta_{12})}{([\eta_{33}(\eta_{11}+\eta_{12})-2\eta_{13}^2])} + 1$, $\varepsilon_{33}^{int\prime} = \frac{(\eta_{11}'+\eta_{12}')}{([\eta_{33}'(\eta_{11}'+\eta_{12}')-2\eta_{13}'^2])} + 1$, $\varepsilon_{33}^{int\prime\prime} = \frac{(\eta_{11}''+\eta_{12}'')}{([\eta_{33}''(\eta_{11}''+\eta_{12}'')-2\eta_{13}''^2])} + 1$ for (001)-, (101)-, and (111)-oriented films, respectively). For (001)-oriented films, the second term can be expanded as $\sum\limits_k P_3^k \frac{d\phi_k}{dE_3} = P_3^1 \frac{d\phi_1}{dE_3} + P_3^2 \frac{d\phi_2}{dE_3}$, where $k = 1$ represents the in-plane polarized a domains and $k = 2$ represents the out-of-plane polarized c domains. For a domains, the polarization along the [001] (P_3^1) is absent which can simplify $\sum\limits_k P_3^k \frac{d\phi_k}{dE_3}$ to be $P_3^2 \frac{d\phi_2}{dE_3}$. In addition, ϕ_2 is known to be $1 - \frac{(s_{11}-s_{12})\left(u_{\rm m}-Q_{12}P_{\rm s}^2\right)}{s_{11}(Q_{11}-Q_{12})P_{\rm s}^2} + \frac{E_3\left(s_{11}^2-s_{12}^2\right)}{s_{11}(Q_{11}-Q_{12})^2 P_{\rm s}^3}$ by minimizing the total free energy, where $P_s = P_3^2$. Thus, $P_3^2 \frac{d\phi_2}{dE_3}$ can be re-written as $\frac{\left(s_{11}^2-s_{12}^2\right)}{s_{11}(Q_{11}-Q_{12})^2 P_{\rm s}^2}$, which is the analytic formula for the motional, extrinsic contribution in (001)-oriented films. For (101)-oriented films, however, the formula of ϕ_k' is very cumbersome after performing the transformation matrix in the free energy of (101)-oriented system. Thus, we only obtained numerical solutions for $\frac{d\phi'_k}{dE'_3}$. For (111)-oriented films, ϕ''_k turns out to be independent on the electric field where $\frac{d\phi''_k}{dE''_3}$ is zero which indicates the absence of motional, extrinsic contributions in (111)-oriented films. Therefore, the intrinsic and the motional, extrinsic contributions to the dielectric permittivity can be calculated numerically in various strain regimes via such thermodynamic analyses. The details regarding the calculation and analysis for the phase diagrams and dielectric response will be discussed in Sec. III and Sec. IV, respectively.

III.PHASE DIAGRAMS OF MONODOMAIN and POLYDOMAIN $PbZr_{1-x}Ti_xO_3$ THIN FILMS

As noted above, few reports (either experimental or theoretical) have discussed any aspect of the strain- and composition-dependence of polydomain structures in (101)- and (111)-oriented $PbZr_{1-x}Ti_xO_3$ films. Thus, to aid the development of the polydomain phase diagrams from the limited resources, we first utilized a monodomain model to provide insights into various phases and structures that are potentially produced in this system. Details of this monodomain model used to extract the equilibrium monodomain phases for (001)-, (101)-, and (111)-oriented $PbZr_{1-x}Ti_xO_3$ films ($0.5 \leq x \leq 1.0$) are provided in the Supplemental Materials. Based on these equilibrium monodomain phases, the polydomain phases were hence evaluated numerically as the equilibrium states which possesses the minimum free energy at a given elastic strain condition and Ti content ($0.5 \leq x \leq 1.0$) using the polydomain model described above.

III.A (001)-Oriented Heterostructures

In (001)-oriented heterostructures, three monodomain phases were found to be present across the range of strain and composition values explored herein: 1) a tetragonal c phase ($P_1 = P_2 = 0, P_3 \neq 0$), 2) a monoclinic r phase ($P_1 = P_2 \neq 0, P_3 \neq 0$), and 3) an orthorhombic aa phase ($P_1 = P_2 \neq 0, P_3 = 0$) in the compressive, intermediate, and tensile strain regimes, respectively, where P_1, P_2, and P_3 are along the crystallographic directions x_1, x_2, and x_3 in reference frame X (x_1, x_2, x_3) (Figure 1(a)). Note that the c phase is energetically favored under large compressive strains since the strain stabilizes the out-of-plane P_3 component. Upon decreasing the compressive strain, the in-plane P_1 and P_2 components appear in the r phase and finally, under the influence of large tensile strains, the structure evolves into the aa phase with pure in-plane components.

Based on these monodomain results, we can further evaluate the polydomain structures. Performing the minimization of $\tilde{F}$ in terms of P_i and ϕ_k for (001)-oriented $PbZr_{1-x}Ti_xO_3$ films at T = 300 K, we acquire results similar to the polydomain phase diagram predicted in prior work.[14] To aid in the discussion, a table (Table II) is provided that indicates the notation which will be used to refer to each phase in the polydomain structures as well as the polarization components and symmetry of that phase. In the polydomain, (001)-oriented heterostructures, seven different, uniquely identifiable phase are observed (here noted in the notation to be used throughout the rest of this manuscript with the corresponding letter in parentheses demarcating the traditional nomenclature used in prior literature as a reference): T_c (c), T_a (a), M_A (r), M_B (r), M_{C1} (ca^*), M_{C2} (ca), M_{C3} (aa^*). Again, specific definition of the polarization components of each phase is provided (Table II) and a schematic illustration of the various phases is provided (Figure 1 (b), note that this illustration schematically shows the orientation of polarization within the unit cell in reference frame X).

The nomenclature used herein is different from the traditionally applied nomenclature for two reasons. First, in the subsequent analysis of (101)- and (111)-oriented heterostructures, no prior nomenclature has been established and thus we provide a unified naming pattern applicable to all systems. Second, the earlier nomenclature of the (001)-oriented heterostructures fails to accurately differentiate some of the subtle differences in structure that are observed. In this regard, we find two different tetragonal phases: one with the polarization along the out-of-plane [001] which we refer to as T_c (c) and one with the polarization in-the-plane along [100] or [010] which we refer to as T_a (a). There are, additionally, a number of phases with monoclinic symmetry (M_A, M_B, and M_{Ci}). The M_A and M_B phases possess polarizations only within $\langle 110 \rangle$ and the M_{Ci} phases possess polarizations only within $\langle 001 \rangle$. The M_A and M_B phases make up what has traditionally been referred to as the r phase, as in polydomain $r_1/r_2/r_1/r_2$ structures. Our studies reveal that it is possible for the polarization to rotate continuously within the $\langle 110 \rangle$ from $0.6 < P_1/P_3 < 1.5$ across the strain range $-2.5\% \leq \varepsilon \leq 2.5\%$ thus leading to two subphases M_A and M_B in the so-called $r_1/r_2/r_1/r_2$ structure. For this work, the M_A and M_B phases are differentiated by the magnitude of the ratio P_1/P_3 which is < 1.0 in the M_A phase but > 1.0 in M_B phase. The M_{Ci} phases make up what has traditionally been referred to as the ca^*, ca, and aa^* phases and in all cases two of the polarization components are non-zero and one is zero. Here the $i = 1, 2, 3$ and it refers to the polarization component that is zero to differentiate the phases.

Based on these calculated phases, we have constructed the composition-strain polydomain phase diagram for (001)-oriented films (Figure 1(c)). In the polydomain system, a single domain T_c phase is present in the compressive strain regime. At intermediate strains, across most of the composition space explored here, a polydomain T_c/T_a ($c/a/c/a$) domain structure is observed. Also at these intermediate strains, when the Ti content $x < 0.6$, a polydomain M_A (or M_B) ($r_1/r_2/r_1/r_2$) domain structure is observed. Furthermore, due to a P_2 instability near the morphotropic phase boundary, the polydomain T_c/T_a ($c/a/c/a$) domain structure evolves into a polydomain M_{C1}/M_{C3} ($ca^*/aa^*/ca^*/aa^*$) domain structure.

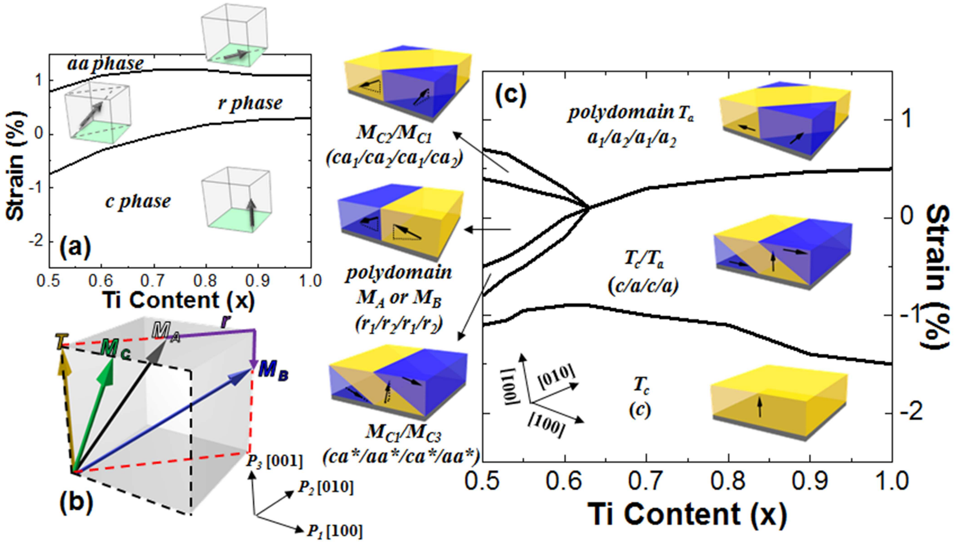

FIG. 1: (a) The composition-strain monodomain phase diagram, (b) the schematic illustration of possible monodomain components in the polydomain structure, and (c) The composition-strain polydomain phase diagram for (001)-oriented films.

TABLE II: The polarization component and the symmetry of all possible monodomain components in the polydomain structure for (001)-, (101)-, and (111)-oriented films.

Orientation	Notation	Polarization Components	Symmetry
(001)	$T_c(c)$	$P_1 = P_2 = 0, P_3 \neq 0$	Tetragonal
	$T_a(a)$	$P_2 = P_3 = 0, P_1 \neq 0\ (a_1);\ P_1 = P_3 = 0, P_2 \neq 0\ (a_2)$	Tetragonal
	$M_A(r)$	$P_1 = P_2 \neq 0 < P_3 \neq 0, 0.60 < P_1/P_3 < 1.0$	Monoclinic
	$M_B(r)$	$P_1 = P_2 \neq 0 > P_3 \neq 0, 1.0 < P_1/P_3 < 1.5$	Monoclinic
	$M_{C1}(ca^*)$	$P_1 = 0, P_2 \neq 0, P_3 \neq 0$	Monoclinic
	$M_{C2}(ca)$	$P_1 \neq 0, P_2 = 0, P_3 \neq 0$	Monoclinic
	$M_{C3}(aa^*)$	$P_1 \neq 0, P_2 \neq 0, P_3 = 0$	Monoclinic
(101)	O	$P_1 = P_2 \neq 0, P_3 = 0$	Orthorhombic
	M_A	$P_1 = P_2 \neq 0, P_3 \neq 0, 0.67 < P_1/P_3 < 0.95$	Monoclinic
	M_{C2}	$P_1 \neq 0, P_2 = 0, P_3 \neq 0, 0.27 < P_1/P_3 < 0.79$	Monoclinic
	T-like M_{C1}	$P_1 \neq 0, P_2 \neq 0, P_3 = 0, 0.001 < P_1/P_2 < 0.19$	Monoclinic
	T-like M_{C2}	$P_1 \neq 0, P_2 = 0, P_3 \neq 0, 0.001 < P_1/P_3 < 0.19$	Monoclinic
(111)	R	$P_1 = P_2 = P_3 \neq 0$	Rhombohedral
	M_{A1}	$P_1 = P_2 \neq 0, P_3 \neq 0, 0.67 < P_1/P_3 < 0.96$	Monoclinic
	M_{A2}	$P_1 = P_3 \neq 0, P_2 \neq 0, 0.67 < P_1/P_2 < 0.96$	Monoclinic
	M_{A3}	$P_2 = P_3 \neq 0, P_1 \neq 0, 0.67 < P_2/P_1 < 0.96$	Monoclinic
	T-like M_{A1}	$P_1 = P_2 \neq 0, P_3 \neq 0, 0.001 < P_1/P_3 < 0.19$	Monoclinic
	T-like M_{A2}	$P_1 = P_3 \neq 0, P_2 \neq 0, 0.001 < P_1/P_2 < 0.19$	Monoclinic
	T-like M_{A3}	$P_2 = P_3 \neq 0, P_1 \neq 0, 0.001 < P_2/P_1 < 0.19$	Monoclinic

At larger tensile strains, a polydomain T_a $(a_1/a_2/a_1/a_2)$ domain structure is stabilized. Similar to what occurred at intermediate strain states, due to a P_3 instability near the morphotropic phase boundary, the polydomain T_a $(a_1/a_2/a_1/a_2)$ domain structure evolves into a polydomain M_{C2}/M_{C1} $(ca_1/ca_2/ca_1/ca_2)$. Overall, across much of the composition and strain space studied herein, with the exception of compositions near the morphotropic phase boundary, a tetragonal symmetry is maintained for the phases. The tetragonal phases can give rise to polydomain structures which are further complicated by the formation of monoclinic structures near the morphotropic phase boundary.

It is worth noting that although it may appear as if we only consider a two-domain configuration in this approach, because of the symmetry of the system and the resulting degeneracy of minority domain structures, extension to a three-domain configuration calculation is

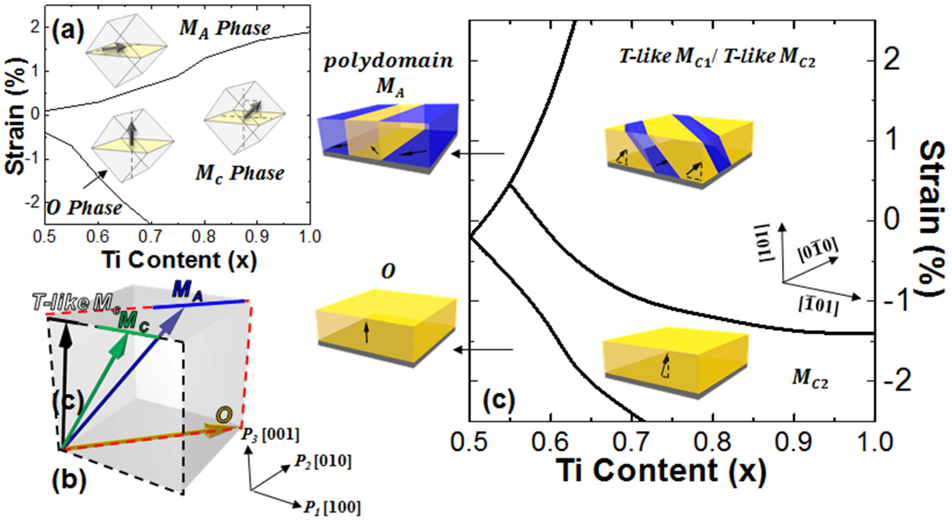

FIG. 2: (a) The composition-strain monodomain phase diagram, (b) the schematic illustration of possible monodomain components in the polydomain structure, and (c) The composition-strain polydomain phase diagram for (101)-oriented films.

redundant as it will provide the same overall fraction of minority domains as we obtain from the two-domain configuration. For instance, the T_c/T_a ($c/a/c/a$) domain structure in (001)-oriented films in reality refers to both polydomain variants $c/a_1/c/a_1$ and $c/a_2/c/a2$ wherein a_1 and a_2 point along P_1 and P_2, respectively. Since a_1 and a_2 are energetically degenerate under the biaxial strain conditions, if a three-domain configuration with a mixture of $c/a_1/c/a_1$ and $c/a_2/c/a_2$ domain structure variants is present, the volume fraction of each polydomain structure should be equal to each other. Thus the total volume fraction of a_1 and a_2 domains in the three-domain configuration is equal to the volume fraction of a_1 or a_2 domain in the case of a two-domain configuration.

III.B (101)-Oriented Heterostructures

In (101)-oriented heterostructures, three monodomain phases were found to be present across the range of strain and composition values explored herein: 1) an orthorhombic O phase ($P_1 = P_2 \neq 0, P_3 = 0$), 2) a monoclinic M_{C2} phase ($P_1 \neq 0, P_2 = 0, P_3 \neq 0$), and 3) a monoclinic M_A phase ($P_1 = P_2 \neq 0, P_3 \neq 0$) in the compressive, intermediate, and tensile strain regime, respectively, where P_1, P_2, and P_3 are along the crystallographic directions x_1, x_2, and x_3 in reference frame X (Figure 2(a)). Note that the O phase is energetically favored under large compressive strains since the strain stabilizes the out-of-plane polarization component. Upon decreasing the compressive strain, the in-plane polarization components appear in the M_{C2} phase and finally the structure evolves into the M_A phase with pure in-plane polarization components as a result of the application of tensile strain.

As we did before, we can leverage these monodomain results to further evaluate the polydomain structures. Performing the minimization of $\tilde{F}'$ in terms of $P_i{}'$ for (101)-oriented $PbZr_{1-x}Ti_xO_3$ films at 300 K, we can generate a composition-strain phase diagram. To aid in the discussion, a table (Table II) is provided that indicates the notation which will be used to refer to each phase in the polydomain structures as well as the polarization components and symmetry of that phase. In the polydomain, (101)-oriented heterostructures, five different, uniquely identifiable phases are observed: O, M_A, M_{C2}, T-like M_{C1}, and T-like M_{C2}. Again, specific definition of the polarization components of each phase is provided (Table II) and a schematic illustration of the various phases is provided (Figure 2(b), note that this illustration schematically shows the orientation of polarization within the unit cell in reference frame X).

In this case, the O phase is found to have non-zero polarization in both the [100] and [010]. Additionally, we differentiate three monoclinic structures. The M_A phase has $P_1 = P_2 \neq 0$, and $P_3 \neq 0$ where $0.67 < P_1/P_3 < 0.95$ and the polarization can only lie within the $\langle 110 \rangle$. The M_{C2} phase has $P_1 \neq 0$, $P_2 = 0$, and $P_3 \neq 0$ where $0.27 < P_1/P_3 < 0.79$ and the polarization can only lie within the $\langle 100 \rangle$. Finally, there are two T-like M_{Ci} phases: T-like M_{C1} ($P_1 \neq 0, P_2 \neq 0, P_3 = 0$) where $0.001 < P_1/P_2 < 0.19$ and T-like M_{C2} ($P_1 \neq 0$, $P_2 = 0$, $P_3 \neq 0$) where $0.001 < P_1/P_3 < 0.19$. The T-like M_{C2} phase is differentiated from the M_{C2} phase in that it can only exist with $0.001 < P_1/P_3 < 0.19$ in the considered strain range ($-2.5\% \leq \varepsilon \leq 2.5\%$). In general, the T-like M_{Ci} phases can be considered as a monoclinically-distorted, but nearly-tetragonal structures with polarization slightly deviating from [010] and [001] for $i = 1$ and 2, respectively.

Based on these calculated structures, we have constructed the composition-strain polydomain phase diagram for (101)-oriented films (Figure 2(c)). In the polydomain system, a monodomain, O-phase region is stabilized under compressive strains and relatively Zr-rich portions of the composition range studied herein. Upon increasing the Ti-content, the structure morphs to the

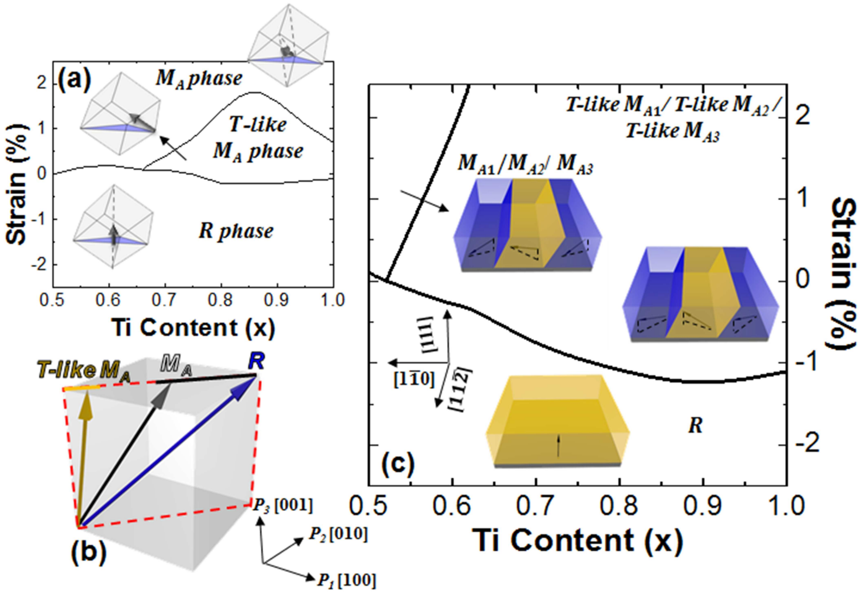

FIG. 3: (a) The composition-strain monodomain phase diagram, (b) the schematic illustration of possible monodomain components in the polydomain structure, and (c) The composition-strain polydomain phase diagram for (111)-oriented films.

M_{C2} phase and a monodomain structure is still maintained. Note that this monodomain M_{C2} phase persists all the way down to small strain regimes at $x < 0.7$. At small compressive and tensile strains, when the Ti content $x \geq 0.65$, the monodomain M_{C2} phase is replaced by a polydomain T-like M_{C1}/T-like M_{C2} domain structure. In the same strain regime, as the composition nears the morphotropic phase boundary, the M_A phase is stabilized and a polydomain M_A structure is formed. Overall, the composition-strain phase diagram of (101)-oriented heterostructures is found to exhibit a fewer number and less variation of stable phases as compared to the (001)-oriented heterostructures within the range of strain and composition considered herein. Additionally, the observed phases in the (101)-oriented films tend to take on monoclinic distortions due to the fact that in-plane misfit strain is akin to a shear strain on the tetragonal $PbZr_{1-x}Ti_xO_3$ unit cell. This is consistent with previously reported experimental observations, where a number of x-ray studies have confirmed the presence of dominant monoclinic symmetry in (101)-oriented $PbZr_{1-x}Ti_xO_3$ films with compositions near the morphotropic phase boundary.[28,29]

III.C (111)-Oriented Heterostructures

In the (111)-oriented heterostructures, three monodomain phases were found to be present across the range of strain and composition values explored herein: 1) a rhombohedral R phase ($P_1 = P_2 = P_3 \neq 0$), 2) a monoclinic T-like M_A phase ($P_1 = P_2 \neq 0$, $P_3 \neq 0$), and 3) a monoclinic M_A phase ($P_1 = P_2 \neq 0$, $P_3 \neq 0$) in the compressive, intermediate, and tensile strain regimes, respectively, where P_1, P_2, and P_3 are along the crystallographic directions x_1, x_2, and x_3 in reference frame X (Figure 3(a)). Note that the R phase is energetically favored under large compressive strains (for all compositions studied herein) since the strain stabilizes the out-of-plane polarization component. Upon transitioning to tensile strain, in-plane polarization components appear and in compositions with higher Ti-content, a T-like M_A phase forms and in compositions with less Ti-content (or at large tensile strains and high Ti-content) a M_A phase is observed.

Based on these monodomain results, we can further evaluate the polydomain structures. Performing minimization of $\tilde{F}''$ in terms of P_i'' at 300 K we can generate yet another composition-strain phase diagram to study the evolution of structure and phases in (111)-oriented films. To aid in the discussion, a table (Table II) is provided that indicates the notation which will be used to refer to each phase in the polydomain structures as well as the polarization components and symmetry of that phase. In the polydomain, (111)-oriented heterostructures, seven different, uniquely identifiable phases are observed: R, M_{A1}, M_{A2}, M_{A3}, T-like M_{A1}, T-like M_{A2}, and T-like M_{A3}. Again, specific definition of the polarization components of each phase is provided (Table II) and a schematic illustration of the various phases is provided (Figure 3(b), note that this illustration schematically shows the orientation of polarization within the unit cell in reference frame X).

In this case, the R phase is found to have non-zero polarization along [100], [010], and [001]. Additionally, although all the monoclinic phases possess polarizations only within $\langle 110 \rangle$, we differentiate the monoclinic structures based on the different P_1/P_3 ratios that are possible. In particular, there are three M_{Ai} phases (M_{A1} ($P_1 = P_2 \neq 0$ and $P_3 \neq 0$) where $0.67 < P_1/P_3 < 0.96$, M_{A2} ($P_1 = P_3 \neq 0$ and $P_2 \neq 0$) where $0.67 < P_1/P_2 <$

0.96, and M_{A3} ($P_2 = P_3 \neq 0$ and $P_1 \neq 0$) where $0.67 < P_2/P_1 < 0.96$) and three T-like M_{Ai} phases (T-like M_{A1} ($P_1 = P_2 \neq 0$ and $P_3 \neq 0$) where $0.001 < P_1/P_3 < 0.19$, T-like M_{A2} ($P_1 = P_3 \neq 0$ and $P_2 \neq 0$) where $0.001 < P_2/P_2 < 0.19$, and T-like M_{A3} ($P_2 = P_3 \neq 0$ and $P_1 \neq 0$) where $0.001 < P_2/P_1 < 0.19$) in the considered strain range ($-2.5\% \leq \varepsilon \leq 2.5\%$). In other words, the T-like M_{Ai} phase is akin to a monoclincially-distorted, tetragonal structure with polarization slightly deviating from [001], [010], and [100] for $i = 1$, 2, and 3 while the M_{Ai} phases possesses a higher distortion and a polarization that can rotate smoothly all the way to the R phase.

Based on these calculated structures, we have constructed the composition-strain polydomain phase diagram for (111)-oriented films (Figure 3(c)). In the polydomain system, a monodomain, R-phase region is stabilized across all compositions under large compressive strains. At Ti-content $x \geq 0.6$ and in both the low compressive and high tensile strain regimes, the T-like M_{Ai} phases are stabilized and a polydomain T-like M_{A1}/T-like M_{A2}/T-like M_{A3} domain structure is created. Under tensile strain and near the morphotropic phase boundary, the M_{Ai} phase is stabilized and a polydomain $M_{A1}/M_{A2}/M_{A3}$ domain structure is generated. In general, the phase diagram of (111)-oriented heterostructures exhibits the least number and variation of stable phases as compared to the (001)- and (101)-oriented heterostructures in the strain and composition range considered herein. Again, it is noted that although a two-domain configuration is directly derived based on the microscopic boundary conditions with equal volume fraction of M_{Ai} (or T-like M_{Ai}) domains, in order to highlight the degenerate nature of all polarization variants, we represent this system as a three-domain configuration with equal volume fraction, which has been experimentally observed in our previous work.[7,8] Additionally, the observed phases in the (111)-oriented heterostructures tend to take on rhombohedral (or monoclinically-distorted versions of rhombohedral) symmetry due to the fact that in-plane misfit strain is akin to a shear strain on the tetragonal $PbZr_{1-x}Ti_xO_3$ unit cell. Again, this is consistent with the previously reported experimental observations, where a number of x-ray studies have also confirmed the presence of dominant rhombohedral symmetry in (111)-oriented $PbZr_{1-x}Ti_xO_3$ films with compositions near the morphotropic phase boundary.[28,29]

IV. DIELECTRIC PROPERTIES OF POLYDOMAIN $PbZr_{1-x}Ti_xO_3$ THIN FILMS

IV.A (001)-Oriented Heterostructures

Having studied the orientation-dependent, composition-strain phase diagrams in polydomain $PbZr_{1-x}Ti_xO_3$ heterostructures, we proceeded to explore the effects of strain, composition, and orientation on the dielectric response. First, we studied the composition-strain map for the intrinsic (Figure 4(a)) and total dielectric response (intrinsic plus extrinsic contributions) (Figure 4(b)) in (001)-oriented heterostructures and obtained similar results to those reported previously.[14,15,30] The maximum intrinsic response is found near the boundary between the polydomain T_a and M_{C2}/M_{C1} structures as a result of the effect of anisotropic dielectric permittivity, where the permittivity measured along the non-polar axis is higher than that measured along the polar axis and thus the T_a structure, with pure in-plane polarization components, has the largest intrinsic response.

As compared to the intrinsic response, in the map of total dielectric response, enhanced effects can be observed in the T_c/T_a, polydomain M_A (or M_B), M_{C1}/M_{C3}, and M_{C2}/M_{C1} structures due to the contribution from extrinsic effects (*i.e.*, domain wall motion). In particular, a large extrinsic contribution is observed in the polydomain M_A (or M_B) structure which leads to the maximum total dielectric permittivity near the multicritical point at the boundary between the five polydomain phases and extending along the boundary between polydomain M_A (or M_B) and M_{C1}/M_{C3} structures due to the presence of opposite signs of out-of-plane polarization in the variants of the polydomain M_A (or M_B) structure which, in

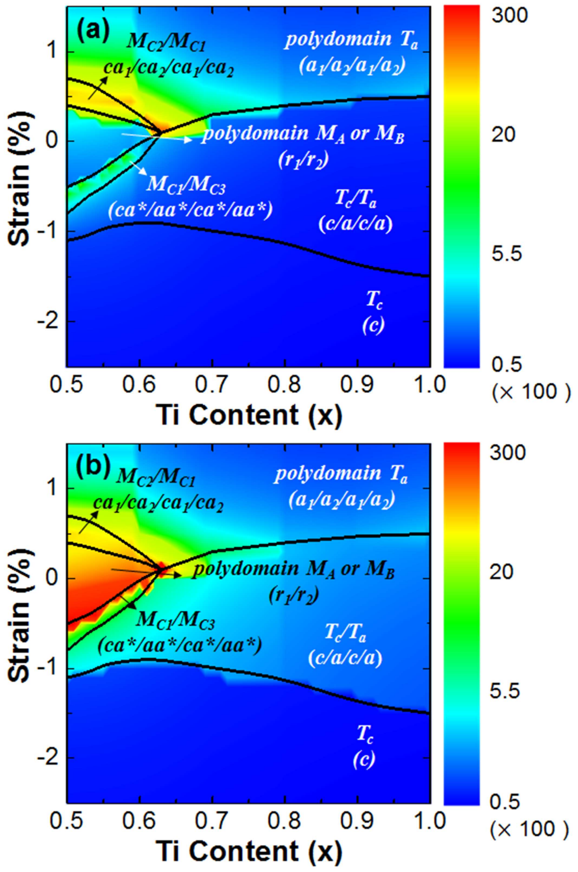

FIG. 4: The composition-strain map for (a) the intrinsic and (b) the total (intrinsic plus extrinsic contribution) dielectric response in (001)-oriented films.

turn, leads to larger field-driven effects in these domain structures. The total dielectric response in the T_c and polydomain T_a domain structures remains the same since there are no domain walls in the T_c region and because of the degenerate nature of the T_a domain variants with respect to the electric field leads to no volume faction change under the electric field.

IV.B (101)-Oriented Heterostructures

We also studied the composition-strain map of the intrinsic (Figure 5(a)) and total dielectric response (intrinsic plus extrinsic contribution) (Figure 5(b)) for (101)-oriented heterostructures. Large intrinsic dielectric response is observed near the phase boundaries between the polydomain M_A, T-like M_{C1}/T-like M_{C2}, and M_{C2} structures, especially in films with lower Ti content and near zero strain, due to the structural instability near the morphotropic phase boundary. As compared to the intrinsic response map, the map of total dielectric response reveals enhanced response in the T-like M_{C1}/T-like M_{C2} structure due to the presence of additional extrinsic contributions from the domain walls. Such extrinsic contributions, however, are found to be less pronounced as the in the related T_c/T_a polydomain structure in the (001)-oriented heterostructures as a result of less preferential alignment of the electric field with a single polarization variant in the (101)-oriented heterostructures which provides less driving force for domain wall motion. The total dielectric response in the monodomain O and M_{C2} regimes remains the same as there are no domain walls present and in the polydomain M_A regime as the degenerate nature of variants in polydomain M_A with respect to the electric field which leads to no volume faction change under application of electric field.

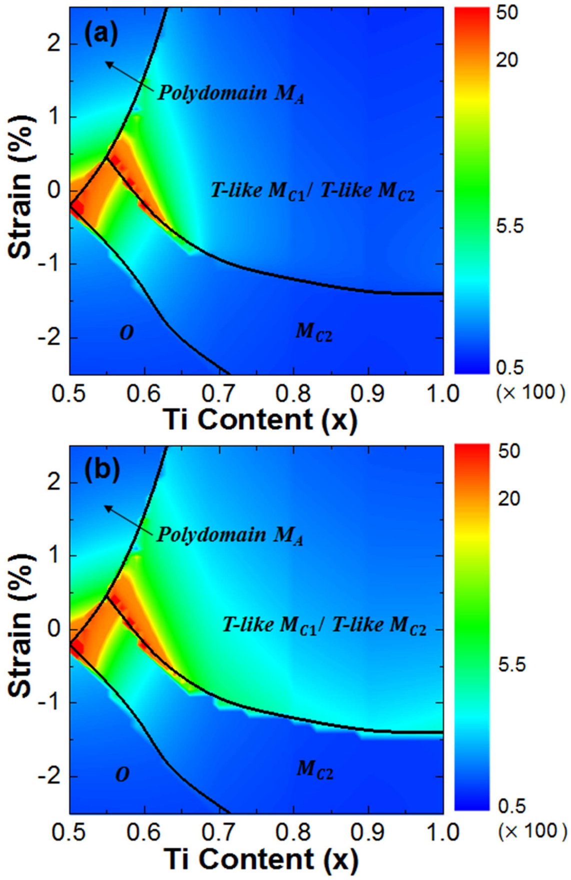

FIG. 5: The composition-strain map for (a) the intrinsic and (b) the total (intrinsic plus extrinsic contribution) dielectric response in (101)-oriented films.

IV.C (111)-Oriented Heterostructures

We also studied the composition-strain map for the total dielectric response (intrinsic plus extrinsic contribution) (Figure 6) in (111)-oriented films. Note that in the (111)-oriented heterostructures, the extrinsic contribution from domain wall motion is not present due to the single-domain nature of the R-phase regime and the degenerate nature of polarization variants in the polydomain T-like M_{A1}/T-like M_{A2}/T-like M_{A3} and $M_{A1}/M_{A2}/M_{A3}$ structures where the structures are made up of equal volume fractions (*i.e.*, 1/3) of the different structural/polarization variants which results in the system having no electric field-driven domain fraction change. This noted, large intrinsic dielectric response can be obtained at the phase boundaries between the T-like M_{A1}/T-like M_{A2}/T-like M_{A3} and the $M_{A1}/M_{A2}/M_{A3}$ phases due to the structural instability near the morphotropic phase boundary. It is also noted that the intrinsic response in the T-like M_{A1}/T-like M_{A2}/T-like M_{A3} regime in the (111)-oriented heterostructures is higher than the related structures in the other orientations (*i.e.*, T_c/T_a polydomain structure in (001)-oriented heterostructures and the T-like M_{C1}/T-like M_{C2} polydomain structures in (101)-oriented heterostructures) due to the anisotropic dielectric response of $PbZr_{1-x}Ti_xO_3$ where the permittivity along the [100] is larger than that along the [001] and thus the intrinsic contribution to permittivity increases as the substrate normal is inclined more towards the [100]. Although the motional extrinsic response is not present in the (111)-oriented heterostructures, which leads to a lower overall response according to our calculation, recent experimental work[7] indicates that (111)-oriented $PbZr_{0.2}Ti_{0.8}O_3$ films can exhibit greatly enhanced dielectric response among (001)-, (101)-, and (111)-oriented versions due to other possible enhancement mechanisms such as stationary domain wall contributions which have not been considered here. This added contribution arises from the fact that high domain wall densities can be achieved in the (111)-oriented heterostructures, thereby adding a new (and still underdeveloped) contribution from the volume domain wall phase in the material. Recent Ginzburg-Landau-Devonshire (GLD) models in $BaTiO_3$, for instance, suggest that such domain walls could give rise to an enhancement of susceptibilities between 1.1 to 1000-times that in the bulk[31] and the experimental work suggests that the domain wall phase has a permittivity 6-70 times that of the bulk of the domain. Addition of such effects into these models will require additional insights into the

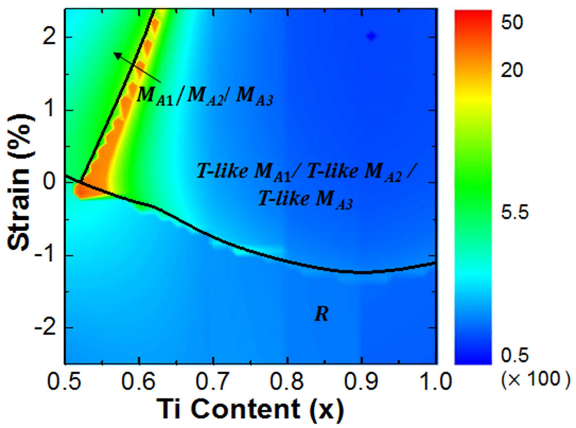

FIG. 6: The composition-strain map for the total (intrinsic plus extrinsic contribution) dielectric response in (111)-oriented films.

nature of this effects and would require more advanced models that can provide realistic domain structures and densities to estimate the volume fraction of domain wall phase.

Overall, we have compared the predicted evolution of dielectric permittivity as a function of strain and composition for (001)-, (101)-, and (111)-oriented polydomain $\mathrm{PbZr}_{1-x}\mathrm{Ti}_x\mathrm{O}_3$ films and here we will highlight some key similarities and differences. First, as is expected, the ferroelectric instability usually results in an enhanced dielectric response and thus irrespective of the film orientation enhanced dielectric permittivity is always present near the phase transition boundary. Second, varying the film orientation can tune the relative fraction of the intrinsic and extrinsic contribution to the dielectric permittivity. For instance, in $\mathrm{PbZr}_{0.2}\mathrm{Ti}_{0.8}\mathrm{O}_3$ films, if we compare the dielectric response of polydomain T_c/T_a structure in (001)-oriented films and its related counterparts, the T-like M_{C1}/T-like M_{C2} structure in (101)-oriented films and the T-like M_{A1}/ T-like M_{A2}/ T-like M_{A3} structure in (111)-oriented films, we can make a few observations. First at a given equivalent misfit strain, the highest intrinsic response is observed in (111)-oriented heterostructures (followed by (101)- and (001)-oriented heterostructures) as a result of the anisotropic dielectric response of $\mathrm{PbZr}_{0.2}\mathrm{Ti}_{0.8}\mathrm{O}_3$ where the permittivity along the [100] is larger than that along the [001] and thus the intrinsic contribution to permittivity increases as the substrate normal is inclined more towards the [100]. This is similar to the monodomain case where the permittivity exhibits higher values along non-polar directions (*i.e.*, [111]) than polar directions (*i.e.*, [001]) in tetragonal ferroelectrics.[32,33] Second, the relative extrinsic contribution (from domain wall motion) to the permittivity decreases as we move from (001)- to (101)-oriented films (as a result of less preferential alignment of the electric field with a single polarization variant) and completely vanishes in (111)-oriented films due to the constant volume fraction of the three polarization variants which is independent of the electric field. Ultimately, the studies indicate that a judiciously chosen combination of elastic strain and film orientation can be used to access a wide variety of structural phase variants and correspondingly diverse dielectric response in ferroelectrics. This knowledge, in turn, can enable the response of a system like $\mathrm{PbZr}_{1-x}\mathrm{Ti}_x\mathrm{O}_3$ to be optimized with relying simply on traditional chemical-routes (*i.e.*, being near to the morphotropic phase boundary).

V. CONCLUSIONS

In this work, we have used a thermodynamic model to calculate the structural phase diagrams and dielectric response in polydomain (001)-, (101)-, and (111)-oriented $\mathrm{PbZr}_{1-x}\mathrm{Ti}_x\mathrm{O}_3$ thin films. Our studies reveal that beyond simple chemistry and strain variations, the use of film orientation can enable dramatic changes in the energetics of the system and thus can be used to tune the structure of the equilibrium phases. In particular, we observe that in (101)- and (111)-oriented films, the stability of the parent T phase is greatly reduced and it tends to evolve into a distorted version. We have observed monoclinic and rhombohedral phases present in the predicted phase diagram of (101)- and (111)-oriented films, respectively, which are consistent with previously reported experimental observations. Additionally, our work provides a theoretical platform by which to systematically optimize the dielectric response in thin films as a function of composition, strain, and orientation. Large dielectric susceptibilities can be found near phase transition boundaries where the ferroelectric instability is induced in these films. At the same time, we also observed that the film orientation can be used to tune the relative fraction of contributions from domain and domain wall motion to the dielectric permittivity. Ultimately, the use of additional orientations of films – beyond the predominantly studied (001)-oriented versions in the literature provide a rich and complex landscape in which we can potentially enhance and gain deterministic control over the properties of materials.

VI. ACKNOLEDGEMENT

R.X. acknowledges the support from the National Science Foundation and the Nanoelectronics Research Initiative under grant DMR-1124696. J.Z. acknowledges support from the National Science Foundation under grant ENG-1434147. Z.C. acknowledges support from the Army Research Office under grant W911NF-14-1-0104. L.W.M. acknowledges support from the National Science Foundation under grant DMR-1149062.

---

[*] Electronic address: `lwmartin@berkeley.edu`

[1] D. G. Schlom, L. Q. Chen, C. -B. Eom, K. M. Rabe, S. K. Streiffer, and J.-M. Triscone, Annu. Rev. Mater. Res. **37**, 589 (2007).

[2] L. W. Martin and D. G. Schlom, Curr. Opin. Solid State Mater. Sci. **16**, 199 (2012).

[3] K. Saito, T. Kurosawa, T. Akai, T. Oikawa, and H. Funakubo, J. Appl. Phys. **93**, 545 (2003).

[4] H. Funakubo, T. Oikawa, S. Yokoyama, K. Nagashima, H. Nakaki, T. Fujisawa, R. Ikariyama, S. Yasui, K. Saito, H. Morioka, H. Han, S. Baik, Y. K. Kima, and T. Suzuki, Phase Transit. **81**, 667 (2008).

[5] J. Ouyang, J. Slusker, I. Levin, D.-M. Kim, C. B. Eom, R. Ramesh, and A. L. Roytburd, Adv. Func. Mater. **17**, 2094 (2007).

[6] Y. H. Chu, M. P. Cruz, C. H. Yang, L. W. Martin, P. L. Yang, J. X. Zhang, K. Lee, P. Yu, L. Q. Chen, and R. Ramesh, Adv. Mater. **19**, 2662 (2007).

[7] R. Xu, J. Karthik, A. R. Damodaran, and L. W. Martin, Nat. Commun. **5**, 3120 (2014).

[8] R. Xu, S. Liu, I. Grinberg, J. Karthik, A. R. Damodaran, A. M. Rappe, and L. W. Martin, Nat. Mater. **14**, 79 (2015).

[9] S. Wada, K. Yako, H. Kakemoto, T. Tsurumi, and T. Kiguchi, J. Appl. Phys. **98**, 014109 (2005).

[10] A. Bernal, S. Zhang, and N. Bassiri-Gharb, Appl. Phys. Lett. **95**, 142911 (2009).

[11] J. Hlinka, P. Ondrejkovic, and P. Marton, Nanotechnology **20**, 105709 (2009).

[12] T. Sluka, A. K. Tagantsev, D. Damjanovic, M. Gureev, and N. Setter, Nat. Commun. **3**, 748 (2012).

[13] N. A. Pertsev, V. G. Kukhar, H. Kohlstedt, and R. Waser, Phys. Rev. B **67**, 054107 (2003).

[14] V. G. Koukhar, N. A. Pertsev, and R. Waser, Phys. Rev. B **64** 214103 (2001).

[15] V. G. Kukhar, N. A. Pertsev, H. Kohlstedt, and R. Waser, Phys. Rev. B **73**, 214103 (2006).

[16] M. D. Glinchuk, A. N. Morozovska, and E. A. Eliseev, J. Appl. Phys. **99**, 114102 (2006).

[17] J. Wang and T. Y. Zhang, Phys. Rev. B **77**, 014104 (2008).

[18] L. Plov, P. Chandra, and K. M. Rabe, Phys. Rev. B **76**, 014112 (2007).

[19] G. Sheng, J. M. Hu, J. X. Zhang, Y. L. Li, Z. K. Liu, and L. Q. Chen, Acta Mater. **60**, 3296 (2012).

[20] Z. G. Ban, S. P.Alpay, J.Appl. Phys. **93**, 504 (2003).

[21] A. K. Tagantsev, N. A. Pertsev, P. Muralt, and N. Setter, Phys. Rev. B **65**, 012104 (2001).

[22] R. Oja, K. Johnston, J. Frantti, and R. M. Nieminen, Phys. Rev. B **78**, 094102 (2008).

[23] Z. Gui, S. Prosandeev, and L. Bellaiche, Phys. Rev. B **84**, 214112 (2011).

[24] J. X. Zhang, Y. L. Li, S. Choudhury, L. Q. Chen, Y. H. Chu, F. Zavaliche, M. P. Cruz, R. Ramesh, and Q. X. Jia, J. Appl. Phys. **103**, 094111 (2008).

[25] N. A. Pertsev, A. G. Zembilgotov, and A. K. Tagantsev, Phys. Rev. Lett. **80**, 1988 (1998).

[26] L. Q. Chen, Landau Free-Energy Coefficients, Physics of Ferroelectrics: A Modern Perspective (Springer-Verlag, Berlin, 2007).

[27] J. S. Speck and W. Pompe, J. Appl. Phys. **76**, 466 (1994).

[28] Y. Li, J. Li, H. Cao, and D. Viehland, Appl. Phys. Lett. **89**, 262905 (2006).

[29] S. C. Ray, H. C. Hsueh, C. H. Wu, C. W. Pao, K. Asokan, M. T. Liu, H. M. Tsai, C. H. Chuang, W. F. Pong, J. W. Chiou, M. H. Tsai, J. M. Lee, L. Y. Jang, J. M. Chen, and J. F. Lee, Appl. Phys. Lett. **99**, 042909 (2011).

[30] J. Karthik, A. R. Damodaran, and L. W. Martin, Phys. Rev. Lett. **108**, 167601 (2012).

[31] Morozovska, A.N., Eliseev, E.A., Varenyk, O.V. and Kalinin, S.V. Effective piezoelectric response of twin walls in ferroelectrics. J. Appl. Phys. **113**, 187222 (2013).

[32] X. H. Du, J. Zheng, U. Belegundu, and K. Uchino, Appl. Phys. Lett. **72**, 2421-2423 (1998).

[33] X. H. Du, U. Belegundu, and K. Uchino, Jpn. J. Appl. Phys. **36**, 5580-5587 (1997).